Theor. Comput. Fluid Dyn.
https://doi.org/10.1007/s00162-024-00714-0

ORIGINAL ARTICLE

Wim M. van Rees

Effect of curvature variations on the hydrodynamic performance of heaving and pitching foils

Received: 31 December 2023 / Accepted: 8 July 2024

Abstract The use of heaving and pitching fins for underwater propulsion of engineering devices poses an attractive outlook given the efficiency and adaptability of natural fish. However, significant knowledge gaps need to be bridged before biologically inspired propulsion is able to operate at competitive performances in a practical setting. One of these relates to the design of structures that can leverage passive deformation and active morphing in order to achieve optimal hydrodynamic performance. To provide insights into the performance improvements associated with passive and active fin deformations, we provide here a systematic numerical investigation in the thrust, power, and efficiency of 2D heaving and pitching fins with imposed curvature variations. The results show that for a given chordline kinematics, the use of curvature can improve thrust by 70% or efficiency by 35% over a rigid fin. Maximum thrust is achieved when the camber variations are synchronized with the maximum heave velocity, increasing the overall magnitude of the force vector while increasing efficiency as well. Maximum efficiency is achieved when camber is applied during the first half of the stroke, tilting the force vector to create thrust earlier in the cycle than a comparable rigid fin. Overall, our results demonstrate that curving fins are consistently able to significantly outperform rigid fins with the same chord line kinematics on both thrust and hydrodynamic efficiency.

Keywords Flapping fin · Morphing fin · Fluid–structure interaction · Curvature variations

1 Introduction

A heaving and pitching fin operating in an incoming flow is an established model system to investigate underwater propulsion as observed in natural fishes [1–3]. Such biologically-inspired propulsion mechanisms offer potential for higher efficiency and agility compared to traditional propellers [4], which can improve ocean exploration, monitoring, and underwater inspection [5,6]. An important aspect of hydrodynamic performance of such systems relates to the interplay between the shape and motion of the fin. Heaving and pitching motions arise in fish fins because of the driving body musculature and the resulting lateral and angular motions of the fish body. On top of that, natural fins deform due to a combination of passive elastic effects associated with the fin softness, and active control associated with the musculature [7–10]. In light of developments in smart, programmable, shape-shifting soft structures on the one side [11,12] and optimization and learning algorithms on the other [13–17], understanding the effect of such curvature variations is crucial to engineer underwater propulsion systems with similar traits.

Communicated by Ashok Gopalarathnam.

W.M.V.Rees (✉)
Department of Mechanical Engineering, Massachusetts Institute of Technology, 77 Massachusetts Avenue, Cambridge 02139, MA, USA
E-mail: wvanrees@mit.edu

Published online: 06 August 2024

The performance of flexible, deforming fins are commonly studied as coupled fluid–structure interaction problems. Most studies have taken this route, with passively deforming fins studied mostly experimentally [18–23] or numerically using potential flow [24–26] or full Navier-Stokes simulations [27–31]. Important quantities that govern the behavior of elastically deforming flapping fins are the relative flexibility of the structure compared to the hydrodynamic loads, the resonance frequency of the fin compared to the dominant frequencies in the loading, and the ratio of foil inertia over the inertia of the flow [32–35]. When the parameters are chosen well with respect to the flow regime, the above works demonstrate that passive flexibility can significantly improve both thrust and efficiency over rigid fins. Further, a significant body of research has shown that non-uniform stiffness distributions in elastically deforming fins can benefit hydrodynamic performance over rigid and uniform-stiffness fins [36–44]. Recently, [45] demonstrated how active control over deformation can lead to increased propulsive performance in heaving fins. Combining active control with passive flexibility, mimicking natural systems [8], could thus lead to performance that can not be achieved with purely passive fins, as well as increase robustness compared to the narrow optimal parameter regime associated a flexible fin [35].

Studying deforming and morphing fins using a fluid–structure interaction approach provides a valuable insights into the forces at play, as well as the power expenditure of the whole system. On the other hand, tackling the coupled fluid–structure interaction problem makes it challenging to isolate the effects of dynamic shape deformations on hydrodynamic performance from the fin's structural properties. In particular, we note that the different structural fin designs and actuation patterns could potentially reach the same dynamic shape variations and thus the same hydrodynamic performance. To provide an alternative, our proposed approach bypasses the fluid–structure interaction problem by looking directly at the effect of imposed, time-varying midline curvature variations on the hydrodynamic performance of flapping foils, following up on our previous work [46]. This approach was also taken in [47] where the authors investigated the optimal curvature phase shift of a plunging foil with curvature variations applied in a 'U' shape, i.e. keeping the chord line of the foil in-line with the flow. They found that optimal performance was achieved when curvature was applied in phase with heave, leading to a 40% efficiency gain compared to the non-curving fin. Further, in [48] the effect of tip curvature on flapping plate performance was investigated experimentally. Here curvature was not dynamically varied throughout the flapping cycle except for snap-buckling plate cases, which were associated with a potential increase in efficiency. Lastly, in our own work [46] we discussed the effect of leading edge curvature variations on 3D flapping fins, both in chordwise and spanwise direction. The chordwise curvature variations were fixed to be in-phase with heave, and only the effect of amplitude was investigated. Nevertheless, possible performance improvements were found of 15% in thrust and 18% in efficiency for the respective optimal curvature amplitudes.

Here we aim to investigate the effect of curvature variations on flapping fin propulsion by varying both curvature amplitude and its phase-shift with respect to the heave motion. This study relies on numerical simulations sweeping a large parameter space, and so we restrict ourselves to a 2D setting. Section 2 will further detail the fin kinematics, flow conditions, and numerical solver as used in this work. In that section we discuss how we distinguish between foils whose curvature variations do not affect chord line kinematics (mode I) and those that do (mode II), with the knowledge that our previous work [46] focused on mode II only. In Sects. 3 and 4 we will discuss the effect of varying the curvature amplitude and phase for mode I and mode II, respectively, and analyze the optimal configurations with respect to thrust and efficiency. Section 5 will compare the results with a similar previous study in 3D [46], and in Sect. 6 we provide conclusions and future perspectives.

2 Methodology

2.1 Fin kinematics

We investigate the effect of curvature variations against a reference rigid fin that moves with harmonic heaving and pitching kinematics:

$$y_{\text{ref}}(t) = A_y \sin(2\pi f t) \tag{1}$$

$$\theta_{\text{ref}}(t) = A_\theta \sin(2\pi f t + \varphi_\theta), \tag{2}$$

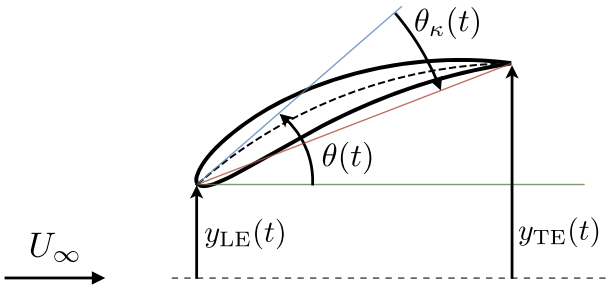

Fig. 1 Definition of the heaving kinematics $y(t)$, the pitching angle $\theta(t)$, and the curvature-induced chord line pitching $\theta_\kappa(t)$. Note that the pitching angle $\theta(t)$ is defined as the angle between the horizontal (green) and the leading edge tangent vector (blue), whereas $\theta_\kappa(t)$ is defined between the leading edge tangent vector and the instantaneous chord line (red). Both angles are positive counter-clockwise. The instantaneous curvature of the fin in this sketch is negative

where f is the flapping frequency, A_y the heaving amplitude, A_θ the pitching amplitude, and φ_θ the phase difference between the heaving and pitching motion. The leading edge of the fin is the center of rotation in all cases. All length scales here are normalized by the chord length c of the fin.

The curvature variations of the fin centerline are described with a simple harmonic function

$$\kappa(t) = A_\kappa \sin(2\pi f t + \varphi_\kappa), \tag{3}$$

with $A_\kappa \geq 0$ the curvature amplitude and φ_κ the phase shift between the *heaving* motion and the curvature. The choice of a constant curvature across the entire chord implies the centerline deforms dynamically into circular arcs of constant arclength c and radii of curvature varying between $\pm A_\kappa^{-1}$ during the cycle.

In this work we define the pitching angle $\theta(t)$ as the angle of the leading edge tangent vector with respect to the horizontal, as shown in Fig. 1. This ensures that the definition of $\theta(t)$ is independent of the actual deformation of the fin. Through the curvature variations, however, the chord line of the fin undergoes angular variations that are different from $\theta(t)$. For a spatially constant, non-dimensional curvature $\kappa(t)$, this additional angle can be expressed as

$$\theta_\kappa(t) = \frac{1}{2}\kappa(t) = \frac{1}{2}A_\kappa \sin(2\pi f t + \varphi_\kappa). \tag{4}$$

For a given choice of pitching angle $\theta(t)$, the trailing edge position is defined as

$$y_{\mathrm{TE}}(t) = y_{\mathrm{LE}}(t) + \frac{\sin(\theta_\kappa(t))}{\theta_\kappa(t)} \sin\left[\theta(t) + \theta_\kappa(t)\right], \tag{5}$$

where $y_{\mathrm{LE}}(t)$ is the vertical position of the leading edge (Fig. 1).

For the deforming fins considered in this work we set $y_{\mathrm{LE}}(t) = y_{\mathrm{ref}}(t)$, and we investigate two choices of the pitching angle variations $\theta(t)$, which we characterize as mode I and mode II. In mode I, we define the pitching angle $\theta(t) \equiv \theta_I(t)$ such that the vertical position of the trailing edge of the curved fin at any time is the same as that of the reference fin, independent of A_κ and φ_κ. This is achieved by setting

$$\theta_I(t) = \theta_{\mathrm{ref}}(t) - \theta_\kappa(t) = \theta_{\mathrm{ref}}(t) - \frac{1}{2}\kappa(t). \tag{6}$$

Curvature variations in Mode I therefore only affect the *camber* of the centerline, while keeping the chord line kinematics identical to those of the reference rigid fin (Fig. 2, left).

In mode II, we align the leading-edge tangent vector with that of the reference fin for any centerline curvature, which is achieved by defining the mode-II pitching angle $\theta(t) \equiv \theta_{II}(t)$ as

$$\theta_{II}(t) = \theta_{\mathrm{ref}}(t), \tag{7}$$

and so the chord line kinematics of these fins will depend on the values of A_κ and φ_κ through Eq. (5) (Fig. 2, right).

In this notation, our previous results [46] correspond to mode II curvature variations with $\varphi_\kappa = 0$. Here we expand by including the mode I results, as well as varying the curvature phase shift φ_κ.

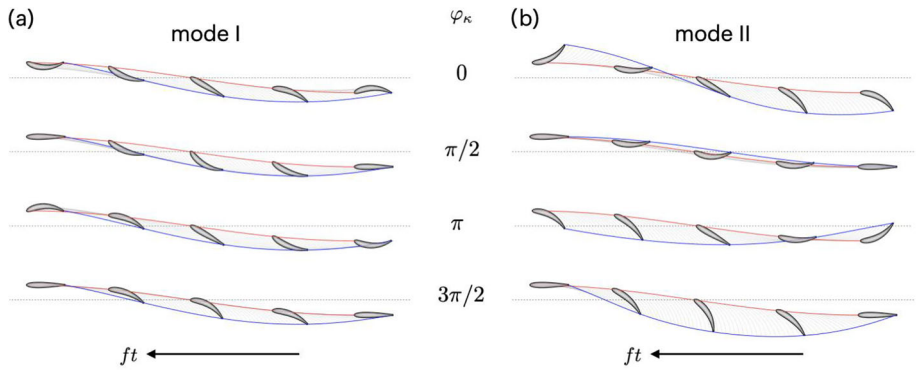

Fig. 2 Overview of fin shapes during the upstroke in mode I (**a**) and mode II (**b**). For this sketch, we choose $A_\kappa = 1$ and four values of φ_κ. The red and blue lines show the trajectory of the leading and trailing edge, respectively. Note that for mode I, the trailing edge trajectory coincides with that of the reference rigid fin for all values of A_κ and φ_κ

2.2 Setup and flow conditions

We immerse the flapping fin in a viscous fluid with kinematic viscosity ν and uniform inflow velocity U_∞. The two non-dimensional parameters governing the flow dynamics of the flapping fin are the Reynolds number $\mathrm{Re} = U_\infty c/\nu$ and Strouhal number $\mathrm{St} = 2A_y f/U_\infty$. In this work we set $\mathrm{Re} = 1500$ and $\mathrm{St} = 0.3$, based on representative regimes investigated in previous studies and deduced from literature. Further, we fix $A_y = 0.4$, $A_\theta = \pi/6$, and $\varphi_\theta = -\pi/2$, for which high propulsive efficiency values were obtained in previous studies [23,49].

We simulate each fin for a duration $0 \leq ft \leq 2$, which was shown to be sufficient for steady-state performance in [46], and extract the time evolution of total force $\boldsymbol{F}(t)$ and power $P(t)$ to define the instantaneous thrust, lift, and power coefficients:

$$C_T(t) = -\frac{\boldsymbol{F}(t)\cdot\hat{\boldsymbol{x}}}{\rho U_\infty^2 c},$$
$$C_L(t) = \frac{\boldsymbol{F}(t)\cdot\hat{\boldsymbol{y}}}{\rho U_\infty^2 c},$$
$$C_P(t) = \frac{P(t)}{\rho U_\infty^3 c},$$

with $\hat{\boldsymbol{x}}$ and $\hat{\boldsymbol{y}}$ the unit vectors in the streamwise and lateral directions. Further, we decompose the instantaneous total force vector into its magnitude, and its relative thrust-component

$$C_T(t) = C_F(t) \cdot \frac{C_T(t)}{C_F(t)},$$

with $C_F(t) = \sqrt{C_T(t)^2 + C_L(t)^2}$ the total instantaneous force coefficient. The ratio C_T/C_F is equivalent to the cosine of the angle of the total force vector with respect to the horizontal. Lastly, mean quantities are computed by integrating over the last half cycle $3/2 \leq ft \leq 2$, and denoted with overlines. The efficiency η is then defined as

$$\eta = \frac{\overline{C_T}}{\overline{C_P}}.$$

In this work, we varied systematically the effect of $A_\kappa \in [0, 1]$ in increments of 0.1, and the effect of $\varphi_\kappa \in [-\pi, \pi)$ in increments of $\pi/4$, for both mode I and mode II.

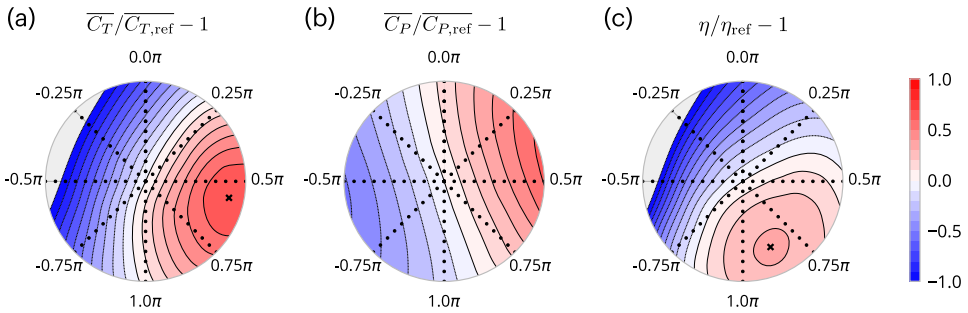

Fig. 3 Mode I results for mean thrust coefficient (**a**), mean power coefficient (**b**), and efficiency (**c**). All coefficients are normalized by the values of the reference rigid fin. The radial axis spans $0 \leq A_\kappa \leq 1$ and the angular axis spans $\varphi_\kappa \in [0, 2\pi)$, so that the reference rigid fin sits at the origin. Black dots represent the individual simulation data points, from which the contours are obtained using interpolation. Each contour plot is clipped to the range $[-1, 1]$ to improve clarity

2.3 Numerical solver

The results are based on numerical simulations of the 2D incompressible Navier–Stokes equations in vorticity-velocity form using a volume penalization technique [50–52]

$$\frac{\partial \omega}{\partial t} + \boldsymbol{u} \cdot \nabla \omega = \nu \nabla^2 \omega + \lambda \nabla \times [\chi (\boldsymbol{u}_s - \boldsymbol{u})] .$$

Here ω is the vorticity field, $\boldsymbol{u}$ the vector velocity field, ν the dynamic viscosity, $\lambda \gg 1$ the penalization parameter, χ the mask field representing the body geometry, and $\boldsymbol{u}_s$ the velocity field inside the body. Here $\boldsymbol{u}_s = \boldsymbol{u}_T + \dot{\theta} \times (\boldsymbol{x} - \boldsymbol{x}_R) + \boldsymbol{u}_{\mathrm{def}}$, with $\boldsymbol{u}_T$ the translational velocity (heave motion), $\dot{\theta}$ the angular velocity (pitching motion), $\boldsymbol{x}_R$ the center of rotation (the leading edge), and $\boldsymbol{u}_{\mathrm{def}}$ the deformation velocity (the curvature variations).

We use a remeshed vortex method as implemented in the wavelet-based block-structured multiresolution adaptive grid solver MRAG-I2D, presented in [53]. The velocity is computed from the vorticity through a multipole method with free-space boundary conditions. Timestepping relies on a second-order Runge–Kutta scheme, with the timestep restricted using the Lagrangian CFL (LCFL) criterion $\Delta t \leq \mathrm{LCFL}/\|\omega\|_\infty$, with $\|\omega\|_\infty$ the maximum instantaneous vorticity in the domain. To compute the forces on the fin we use the projection scheme as described in [54]. Overall, the algorithm and solver reach between first and second order accuracy in space and time and have been extensively validated and used for a range of flow simulations with moving and deforming bodies [13–16,55,56].

For the simulations in this work, we set $\mathrm{LCFL} = 0.1$, use penalization parameter $\lambda = 10^4$, and refinement and coarsening thresholds of 10^{-3} and 10^{-5} respectively. The simulations are run within a unit-square block-structured domain with smallest grid spacing $h_{\min} = 1/8192$. Within this domain, we use a fin chord length $c = 0.05$, flapping frequency $f = 0.375$, and free-stream velocity $U_\infty = 0.05$. In the results below, however, we only report non-dimensional quantities.

3 Effect of mode I curvature variations

In this and the next section, we present the combined effect of $(A_\kappa, \varphi_\kappa)$ in polar contour plots (see Fig. 3 for mode I results). In these plots, concentric circles correspond to keeping A_κ fixed and varying φ_κ, and radial spokes correspond to variations of A_κ at a fixed φ_κ. The rigid fin corresponds to the origin. Values in between simulation points, as well as the optimum parameter combinations, are estimated through quadratic interpolation.

For Mode I curvature variations, Fig. 3 shows the contour plots of $\overline{C_T}$, $\overline{C_P}$, and η, with all values normalized to those of the rigid fin. Generally, the thrust (Fig. 3a) increases with increasing curvature when the phase shift is close to $\phi_\kappa \sim \pi/2$, i.e. when the curvature is in-phase with the pitching kinematics. Increasing curvature with opposite phase shift, $\phi_\kappa \sim -\pi/2$, eventually leads to drag generation, as $\overline{C_T}$ reduces below zero. The power coefficient trend (Fig. 3b) is roughly similar to that of the thrust coefficient, though qualitatively the power contours are slightly rotated counter-clockwise compared to the thrust contours. The efficiency (Fig. 3c),

Table 1 Optimal parameter values for mode I and mode II curvature variations

Case	A_κ	φ_κ/π	$\overline{C_T}$	$\overline{C_P}$	η
Rigid	0	–	0.23	0.93	0.25
Mode I max C_T	0.85	0.56	0.39	1.35	0.29
Mode I max η	0.71	0.87	0.31	0.95	0.33
Mode II max C_T	0.63	0.23	0.41	2.16	0.19
Mode II max η	0.48	0.80	0.13	0.33	0.39
κ-pitch max C_T	0.63	0.23	0.36	1.84	0.20
κ-pitch max η	0.48	0.80	0.078	0.27	0.29

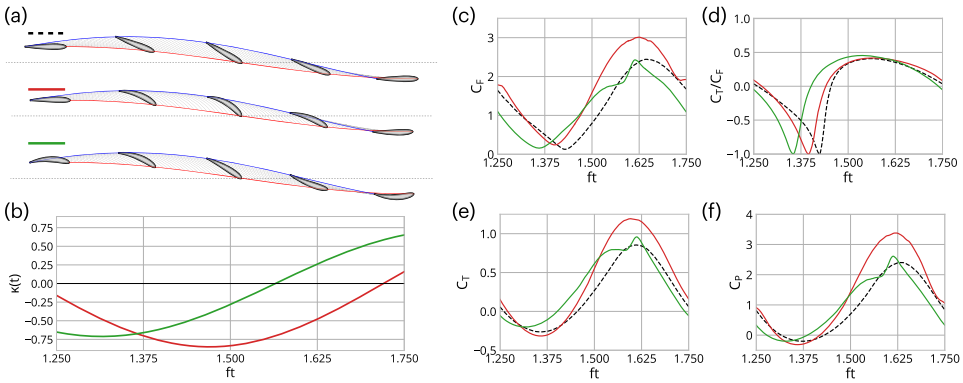

Fig. 4 Results as a function of the non-dimensional time ft during one downstroke for the rigid fin (black dashed), the max-C_T mode I fin (red), and the max-η mode I fin (green). **a** Shape of the fin, **b** curvature $\kappa(t)$, **c** force magnitude coefficient $C_F(t)$, **d** relative thrust component $C_T(t)/C_F(t)$, **e** total thrust coefficient $C_T(t)$ and **f** the total power coefficient $C_P(t)$

which is the ratio of thrust over power coefficients, is therefore maximized towards $\phi_\kappa \sim \pi$. From the contour plots, we extract the parameters associated with maximum $\overline{C_T}$ and maximum η, and report those together with their performance metrics in Table 1. Fig. 4 shows the shape of the fin,curvature, and the evolution of $C_F(t)$, $C_T(t)/C_F(t)$, $C_T(t)$, and $C_P(t)$ during the downstroke $1.25 \leq ft \leq 1.75$ for the reference rigid fin (blue), the high $\overline{C_T}$ fin and the high η fin. In discussing the results, for simplicity we focus on this downstroke.

3.1 Maximum thrust

The maximum thrust fin has about 70% higher mean thrust than the rigid fin. Its curvature variations are characterized by $\varphi_\kappa \approx \pi/2$ (Table 1), so that the maximum curvature is achieved at the zero heave point, half-way through the stroke. At this point, the camber associated with this fin resembles that of a standard, favorably cambered static airfoil. During the downstroke, the curving fin achieves a significantly larger force vector compared to the reference rigid fin as evidenced by the plot of C_F (Fig. 4c, red lines). This increased force magnitude is the main driver of thrust enhancement, as the orientation of the force vector C_T/C_F is practically identical to the rigid fin (Fig. 4d). In physical terms, this implies that the curving fin is simply able to generate a larger overall force vector during its cycle, without drastically altering the underlying mechanism. This is further reflected by the proportional increase in power coefficient over the rigid fin, so that the efficiency almost remains unchanged.

The vorticity field (Fig. 5) shows that the centerline camber induces a strong separation during each stroke, which is largely absent from the rigid fin. Notably, the separation leads to a leading edge vortex (LEV) that is situated on the pressure side of the foil, so that purely in isolation its signature in the pressure distribution would reduce the overall force generated [57] – we denote it a 'pressure-side LEV' (P-LEV). From the force computations, however, we know that the curving fin generates significantly more thrust than the rigid fin, indicating that the negative effects of the P-LEV are countered by a more favorable pressure distribution on the suction side of the foil. During the downstroke the P-LEV is generated around $ft = 1.35$, just after the heave reversal. The vortex then moves downstream while remaining attached to the fin during the stroke. It is shed around $ft = 1.75$, almost perfectly coinciding with the end of the downstroke. The evolution of $C_F(t)$

shows a small plateau around this time in Fig. 4b, though this is not reflected in the thrust curve since C_T/C_F is approximately zero around this time.

Remarkably, the mean power consumption of this mode I maximum thrust fin increases at a slower rate than the mean thrust increasing, leading to a 16% increase in efficiency over the reference rigid fin.

3.2 Maximum efficiency

The maximally efficient fin has curvature parameters $(A_\kappa, \varphi_\kappa) \approx (0.7, 9\pi/10)$ (Table 1), so that the maximum curvature in this fin is reached slightly later than the heave reversal. This case realizes a 32% higher efficiency than the rigid fin, which is achieved through a similar mean power expenditure but about 35% higher thrust generation. This is a striking result, where two fins with the same leading and trailing edge kinematics, and a very similar power consumption, can have significant changes in thrust coefficient just by virtue of dynamic camber variations.

Examining the time evolution of C_T/C_F and C_T (Fig. 4d,e, green lines), we observe that the max-η fin starts generating thrust earlier in the cycle compared to the rigid fin (black lines). This occurs because its maximum curvature is achieved at $ft = 1.315$, so that thrust can be generated at the lower apparent angles of attack in the first half of the downstroke. This early presence of camber also leads to a lower drag coefficient on the fin during the immediate onset of the stroke, which increases the overall mean thrust coefficient. The max-η fin also has much smaller 'losses' during the reversal of the motion at the start and end of the stroke, as measured by the power required at these times. By curving, the fin is thus able to achieve the rotational motion with much less additional power input compared to the rigid fin.

The vorticity field (Fig. 5) shows that the max-η fin generates a pressure-side leading edge vortex (P-LEV) around $ft = 1.25$, just at the beginning of the downstroke. The P-LEV is formed from a region of leading edge flow separation, induced by the combination of pitching acceleration and the foil's camber. During the downstroke, the vortex remains attached and travels backwards towards the leading edge. It sheds from the trailing edge around $ft = 1.6$. The vortex shedding is observed in the plots of C_F as a small plateau followed by a local peak in the total force. Qualitatively, the force bump can be related to the adverse signature of the P-LEV on the pressure distribution; as the vortex is shed, the disadvantageous low-pressure region associated with it moves away from the foil. This directly translates to a large instantaneous C_T value, since the orientation of the force vector C_T/C_F almost maximally benefits thrust generation at this time. The max-η foil stops generates positive thrust at an almost identical time instance as the rigid fin. Together with the early onset of thrust generation, this leads to a significantly larger mean thrust coefficient of the max-η foil.

4 Effect of mode II curvature variations

Before analyzing the Mode II curvature variations, we recall that the curvature parameters effectively alter both the effective pitch angle of the chord line, as well as the fin camber. It is therefore instructive to compare each mode II curving fin with a non-curving fin with identical chord line kinematics. Following [46] this configuration is denoted the κ-pitch fin, and the results are obtained by simulating a rigid fin whose pitching kinematics follow from adding the expression for $\theta_\kappa(t)$ in Eq. (4) to the pitch angle $\theta_{\text{ref}}(t)$ in Eq. (2). The pitching kinematics of these rigid κ-pitch fins are therefore functions of the parameters A_κ and φ_κ. With this

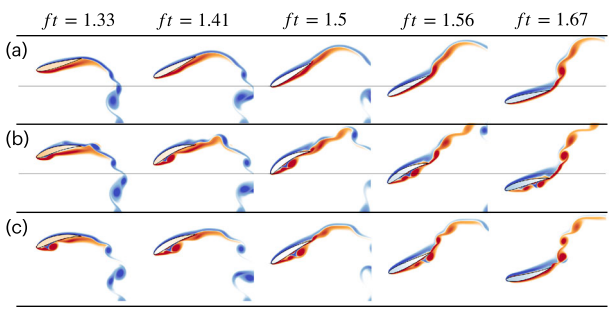

Fig. 5 Vorticity field at five instances during the downstroke for the rigid (**a**) and the mode-I max-C_T (**b**) and max-η (**c**) fins

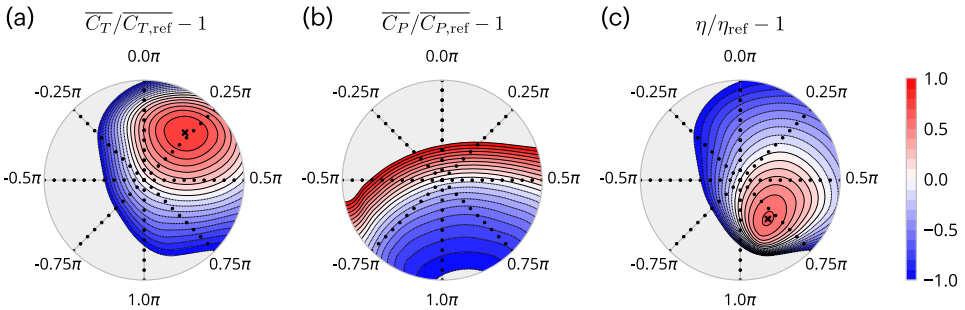

Fig. 6 Mode II results for mean thrust coefficient (**a**), mean power coefficient (**b**), and efficiency (**c**) for the curving fin in mode I. All results are normalized by the values of the reference rigid fin. The radial axis spans $0 \leq A_\kappa \leq 1$, whereas the angular axis spans $\varphi_\kappa \in [-\pi, \pi)$, so that the reference rigid fin sits at the origin. Black dots are the individual simulations. Each contour plot is clipped to the range $[-1, 1]$ to improve clarity

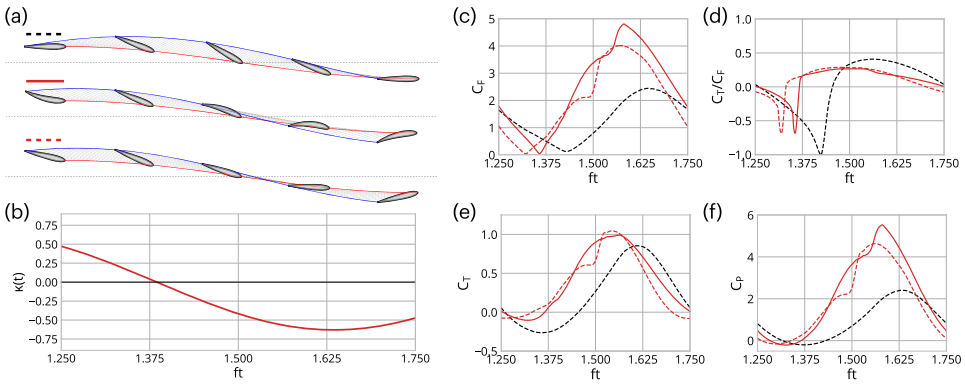

Fig. 7 Results as a function of the non-dimensional time ft during one downstroke for the rigid fin (black dashed), the max-C_T mode II fin (red), and the κ-pitch fin with the same parameters as the max-C_T fin (dashed red). **a** shape of the fin, **b** curvature $\kappa(t)$, **c** force magnitude coefficient $C_F(t)$, **d** relative thrust component $C_T(t)/C_F(t)$, **e** total thrust coefficient $C_T(t)$ and **f** the total power coefficient $C_P(t)$

perspective, any mode II curvature variation can be interpreted as a mode I curvature variation on top of the associated κ-pitch rigid fin.

Figure 6 shows the contour plots of the effect of mode II curvature variations on thrust, power, and efficiency. Compared to mode I, the region of improved thrust over the reference fin is much narrower, spanning only a quadrant between, roughly, $0 \leq \phi_\kappa \leq \pi/2$. Within this region, we find a maximum at $A_\kappa = 0.63$, with thrust decreasing as A_κ increases further. The power coefficient plot shows that power changes substantially when the phase shift is around $\varphi_\kappa \sim 0 \pm \pi$, i.e. when curvature variations are in phase with heave. In a substantial region of the parameter space (in gray) the mean power consumption is over twice that of the reference fin, due to the very large trailing edge amplitudes associated with the curving fins. The efficiency has a narrow peak around $\phi_\kappa \sim 3\pi/4$. The optimum parameter combinations for thrust and efficiency are highlighted with crosses, and their associated performance values are listed in Table 1. For each of these optimum values, we also simulated the associated κ-pitch fins. Figure 7 shows the time evolution of the forces and power for the rigid fin (black dashed), the maximum thrust mode II curving fin (red), and the κ-pitch rigid fin associated with the maximum thrust parameters (red dashed). Figure 8 shows the quantities for the maximum efficiency mode II curving fin (green), and the κ-pitch rigid fins associated with the maximum efficiency parameters (green dashed). For each of the hydrodynamic performance metrics, we will discuss first the effect of the pitching angle by comparing the reference fin results (dashed black lines) to the κ-pitch rigid fin results (dashed red/green lines). Subsequently, we will analyze the effect of curvature variations by comparing the mode II curving fin results (solid red/green lines) to the κ-pitch fin results (dashed red/green lines).

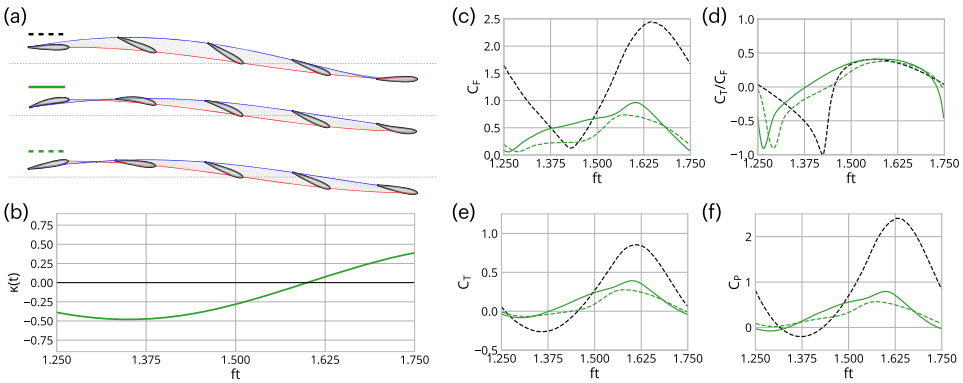

Fig. 8 Results as a function of the non-dimensional time ft during one downstroke for the rigid fin (black dashed), the max-η mode II fin (green), and the κ-pitch fin with the same parameters as the max-η fin (dashed green). **a** Shape of the fin, **b** curvature $\kappa(t)$, **c** force magnitude coefficient $C_F(t)$, **d** relative thrust component $C_T(t)/C_F(t)$, **e** total thrust coefficient $C_T(t)$ and **f** the total power coefficient $C_P(t)$

4.1 Maximum thrust – effect of pitching kinematics

The κ-pitch fin with the maximum thrust parameters (red dashed lines) achieves about 56% more thrust, at roughly twice the power expenditure, compared with the reference rigid fin (black dashed lines). For these parameters, the additional term in the pitching kinematics of the κ-pitch fin, described by Eq. (4), has an amplitude of about 60% of A_θ, and a phase shift of close to 45 degrees. Consequently, the κ-pitch starts its downstroke at $ft = 1.25$ with a higher pitching angle and so is able to generate thrust earlier in the stroke than the reference rigid fin. The overall force vector has a much larger magnitude and peaks earlier in the stroke, both of which can be attributed to the larger trailing-edge velocity for the κ-pitch fin compared with the rigid reference fin at this time [2,58]. The κ-pitch fin also generates a very strong pressure-side leading edge vortex (P-LEV) early on in the stroke (Fig. 9b). This P-LEV gets shed already around $ft = 1.5$, half-way during the downstroke, and this event registers as a local peak in the force and thrust evolution at this time. In the second half of the downstroke, the κ-pitch fin begins to reverse its pitching angle, reaching a zero-pitch value around $ft = 1.65$ compared to $ft = 1.75$ for the reference rigid fin. This leads to a significantly smaller C_T/C_F ratio and C_T value in this part of the stroke, as the force vector is angled more upright. Overall, the first half of the stroke is associated with much larger forces and a wide window of thrust generation. The second half of the stroke, however, is associated with high power consumption and low efficiency. Consequently, the entire stroke requires about twice the energy of the rigid fin to sustain, leading to a 20% reduction in efficiency compared with the rigid fin.

4.2 Maximum thrust – effect of curvature

Compared to the κ-pitch fin (Fig. 7, dashed red lines), the curvature variations of the max-C_T mode II motion (Fig. 7, solid red lines) lead to about 14% more thrust with about 17% higher mean power consumption, so that the efficiency drops slightly to 0.19. Specifically, the curving fin gains thrust over the rigid κ-pitch fin in two ways: first because the curvature reduces the strength of the P-LEV, and second through a favorable camber in the second half of the stroke that provides an increase in the overall force vector as well as the C_T/C_F ratio.

The flow fields of the maximum thrust cases (Fig. 9b,c) illustrate the differences in the P-LEV dynamics. The curvature of the mode II curving fin during the first half of the downstroke leads to a smaller effective inflow angle, reducing the strength of the separated vortex compared to the κ-pitch fin. Around $ft = 1.5$ the strong P-LEV on the κ-pitch fin has traveled towards the trailing edge and induces a small plateau in the the thrust (see Fig 7e) compared to the curved fin. After the vortex is shed, the thrust coefficient increases again before decreasing as the stroke reverses. For the mode II curving fin the curvature shifts the plateau to a slightly later time, when C_T/C_F is smaller, and the reduction in the strength of the P-LEV further diminishes its effect. Consequently, the mode II curving fin is able to somewhat reverse the performance decrease associated with the p-LEV of the κ-pitch fin, which leads to the observed higher thrust coefficient of the curving fin.

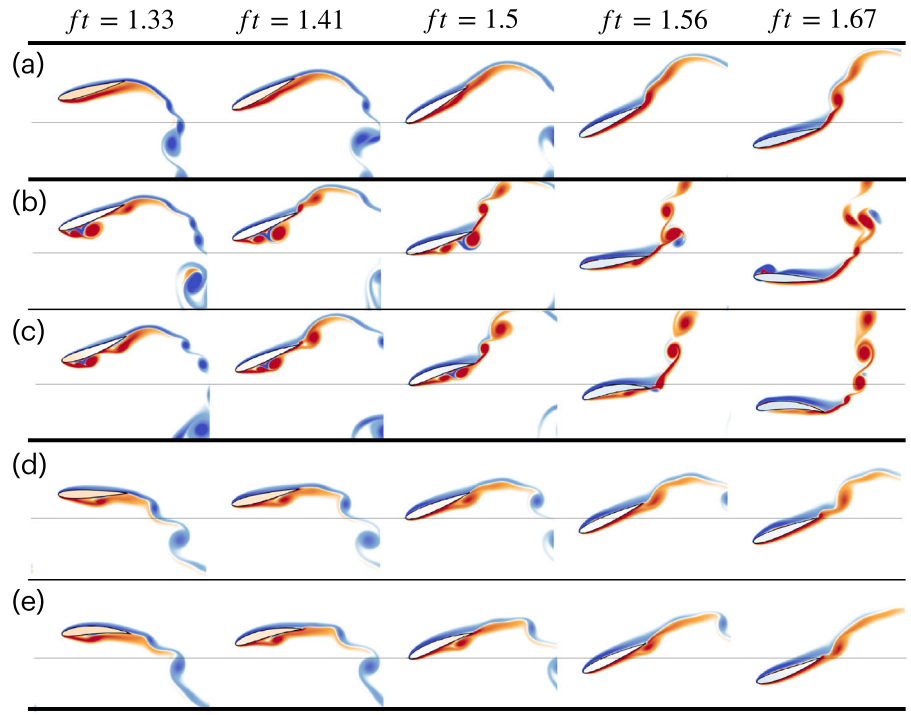

Fig. 9 Vorticity field at five instances during the downstroke for the reference rigid fin (**a**), the max-C_T rigid κ-pitch fin (**b**), the max-C_T mode II curving fin (**c**), the max-η rigid κ-pitch fin (**d**), and the max-η mode II curving fin (**e**)

4.3 Maximum efficiency – effect of pitching kinematics

Both the curving and the κ-pitch mode II high efficiency fins use a drastically different mechanism compared with all other fins. The phase shift of the curvature variations φ_κ is $8\pi/10$, which means that the pitching term due to curvature has a phase difference with respect to the reference pitching term of about $\pi/4$. Further, the amplitude is about half of A_θ. The maximum velocity of the fin trailing edge is about 50% smaller than that of the reference fin, and consequently the mean thrust coefficient is about three times smaller. In fact, the maximum trailing edge excursion and velocities are very similar to those of the leading edge. With this motion, the power coefficient drops disproportionally larger than the thrust coefficient, leading to a gain in efficiency over the reference rigid fin by about 16%. Given that the reference rigid fin and the high-efficiency κ-pitch fin operate in very different regimes, diving further into a direct comparison is not deemed insightful. Instead, we focus in the next subsection on the difference between the max-η κ-pitch fin and the associated mode II curving fin to investigate the effect of curvature in this state of the system.

4.4 Maximum efficiency – effect of curvature

Within the low-thrust regime of the mode II κ-pitch fin (Fig. 8, dashed green), the curvature variations of the curving mode II fin (solid green) have a significant effect. With dynamically changing curvature, the thrust coefficient increases by almost 70% while the power coefficient increases by 35%, leading to a net efficiency gain of 35%. The force curves indicate that the most significant increase in thrust is attained in the middle part of the downstroke, for $1.375 \leq ft \leq 1.625$. This can be attributed to the favorable camber in this part of the stroke which causes earlier thrust generation in the stroke, and also increases the total force coefficient, both benefiting the overall mean thrust generation. Despite the earlier onset of thrust generation, the curving fin is able to generate positive thrust until the end of the stroke, similar to the κ-pitch fin. These positive effect of curvature are very similar to those observed for the mode I maximum curvature fins, despite the very different pitching kinematics of these two cases.

Around $ft = 1.5$ the κ-pitch fin sheds the P-LEV, which increases the overall force and thrust coefficient during that time. However, the overall values still remain below that of the curving fin. Towards the end

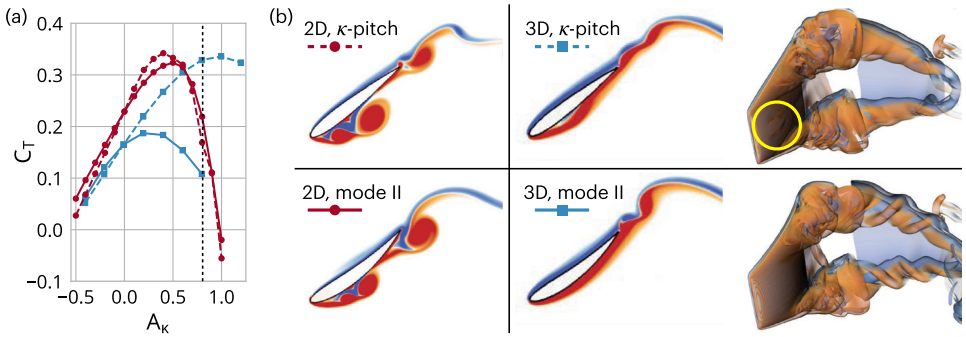

Fig. 10 **a** Thrust coefficient as a function of A_κ for $\varphi_\kappa = 0$, showing 2D (red, circles) and 3D (blue, squares) results for mode II curving (solid) and κ-pitch (dashed) fin. **b** Vorticity field at $ft = 1.4$ of 2D simulations (middle) and 3D simulations (right) for the κ-pitch fin (top) and the mode II curving fin (bottom) with $A_\kappa = 0.8$, $\varphi_\kappa = 0$. The 3D simulation results contain the center-plane vorticity field as well as a volume rendering of the 3D vorticity field - the yellow circle in the latter (top-right) highlights the LEV

of the stroke, a new LEV is generated on the suction side of the κ-pitch fin, which leads to larger overall force coefficient during the reversal of the heave motion than for the curving fin. This force has a negligible component in the flow direction, though, and thus does not contribute to thrust.

5 Comparison with 3D results

In a previous study [46], we simulated a 3D trapezoidal fin with an average aspect ratio close to one, under the exact same flow conditions and heaving/pitching kinematics as used here. We tested in that work only mode II variations with $\varphi_\kappa = 0 \pm \pi$, and varied A_κ within the same range observed here.

Analyzing the subset of 2D data within this parameter range demonstrates a qualitative difference with the 3D results (Fig 10, a). In 3D, we found that the κ-pitch fin significantly outperforms both the reference *and* the mode II curving fin on thrust coefficient at large values of A_κ. In fact, the largest thrust coefficient overall was found to correspond to the 3D κ-pitch fin at $A_\kappa = 1.0$, corresponding to $C_T = 0.33$, whereas the 3D curving fin peaked at $A_\kappa = 0.28$ with $C_T = 0.19$. In contrast, our 2D results at fixed $\varphi_\kappa = 0$ show that both the κ-pitch and the curving fin share a peak thrust coefficient at $A_\kappa \approx 0.4 - 0.5$, with value of $C_T \approx 0.32 - 0.33$. A direct comparison of the numerical values of thrust coefficient between 2D and 3D is not insightful, so instead we focus on discussing the qualitative differences in these trends.

The explanation for this discrepancy can be related to the difference in LEV dynamics between the 2D and 3D cases. Figure 10b compares the vorticity field of the 2D simulations (left) with that in the center-plane of the 3D simulations (middle) and the 3D vorticity field (right). The snapshots are taken at $ft = 1.4$ for the case $A_\kappa = 0.8$, $\varphi_\kappa = 0$. The top and bottom rows correspond to the κ-pitch fins and mode II curving fins, respectively. For the κ-pitch fin, the 3D P-LEV (circled in yellow) is strongly suppressed compared to 2D. For the mode II curving fin, the P-LEV is completely absent in 3D. This points to a drastic effect of finite aspect ratio on the LEV development, consistent with results on linearly accelerating 3D wings [59], where for small aspect ratios the induced velocity of the tip vortices keeps the leading edge vortex sheet from separating. Since in our context the P-LEV reduces the overall performance of the fin, the 3D fin has the ability to increase the curvature (and hence the effective pitch angle) far beyond the angles where leading edge separation occurs in 2D. At these large angles, the difference between the κ-pitch fin and mode II curving fin performance can be related to differences in drag and effective heave-pitch kinematics, as discussed in [46]. In contrast, in 2D the presence of the P-LEV for both the κ-pitch and the curving fin dominates and aligns their respective hydrodynamic performances.

6 Conclusion

We performed a systematic investigation on the effect of centerline curvature variations on the hydrodynamic performance of flapping foil propulsion.

For mode I variations the chord line kinematics of the curving fin remain identical to the reference rigid fin. The results show that mode I curvature variations, when applied with a phase shift of around $\pi/2$ (roughly

in-phase with pitch) and curvature amplitude of 0.85, can improve mean thrust generation by about 70% over a rigid fin. The thrust increase is related to an overall increase of the hydrodynamic force vector due to the fin's favorable camber during the up- and downstrokes. Though the average hydrodynamic power of the curving fin increases as well, it does so at a smaller rate leading to an overall efficiency improvement of about 16%. When the mode I curvature variations are applied with a phase-shift of around $9\pi/10$ (roughly in-phase with heave) and curvature amplitude of 0.7, the efficiency of the curving fin can improve by about 32% over a reference rigid fin. This gain is achieved because the fin generates about 35% higher thrust for the same average power coefficient as the rigid fin. The higher thrust is predominantly achieved during the first half of each up- or downstroke, where the favorable camber angles the force vector more forward compared to a rigid fin. The associated increase in power expenditure is offset by lower power losses during the heave-motion reversal, aided by the force vector orientation during these phases. For both the maximum thrust and maximum efficiency cases, a pressure-side leading edge vortex (P-LEV) is present during the first half of the up- and downstrokes, though it does not prevent these fins from outperforming the rigid reference fin.

For mode II curvature variations, consistent with [46], the high thrust performance is mostly due to beneficial heaving-pitching kinematics and can in large part be reproduced by a rigid fin with the same chord line motion. There is a small but favorable effect of camber variations on top of these chord line motions, which are largely related to a reduction in the pressure-side leading edge flow separation. Compared to the mode I results, the best mode II fins achieve slightly larger thrust coefficients but at significantly lower values of efficiency. In contrast, the largest efficiency results in the mode II curving motions are obtained for significantly lower thrust coefficients compared to the rigid fin. In these cases, the effective pitch angles are much smaller than for the rigid reference fin. Still, the results show that camber variations can significantly improve performance compared to a rigid fin with identical chord line kinematics. The maximum efficiency with mode II curvature has a value of 39%, outperforming all other fins. Compared to the rigid κ-pitch fin with identical chord line kinematics, the efficient curving fin is able to achieve 67% larger thrust by applying favorable camber during the up- and downstroke. Overall, our results show the impact on hydrodynamic performance of fin curvature variations across a range of phase shifts and amplitudes. The results demonstrate that curving fins are consistently able to significantly outperform rigid fins with the same chord line kinematics on both thrust and hydrodynamic efficiency. We expect our results to provide a basis for comparing fluid–structure interaction (FSI) results, where the kinematics of any passively or actively deforming fin may be projected onto the curvature parameters defined here. Further, we believe our optimally curving fins can serve as a design target or constraint for optimization studies, reducing the complexity of FSI inverse problems.

In future work, we will focus on more complex spatial curvature profiles in light of reported benefits of non-uniform stiffness distributions. Given our results, we hypothesize that spatially non-uniform curvature variations could provide a pathway to suppressing the unfavorable leading edge flow separation and associated P-LEV, and thus further improve the performance of curving fins compared to the reference rigid fin.

Acknowledgements We gratefully acknowledge support from the American Bureau of Shipping through a Career Development Chair, and from the MIT Sea Grant College Program through the Doherty Professorship in Ocean Utilization. We further thank Dr. David Fernández-Gutiérrez for helpful discussions in the early stages of this work.

Author contribution W.M.v.R. performed all work.

Funding 'Open Access funding provided by the MIT Libraries' Funding for this work was received from the American Bureau of Shipping through a Career Development Chair, and from the MIT Sea Grant College Program through the Doherty Professorship in Ocean Utilization.

Declarations

Data availability Data and materials are available on request to the author.

Ethical approval Not applicable

Appendix A: Effect of curvature on trailing edge location

Consider the centerline of the fin as an inextensible planar curve with normalized arclength parametrization $\boldsymbol{r}(s)$ with $0 \leq s \leq 1$. To remove the effect of externally imposed heave and pitch, we set the leading edge position $\boldsymbol{r}(0) = \boldsymbol{0}$ and leading edge tangent vector $\boldsymbol{r}'(0) = \hat{\boldsymbol{e}}_x$, with $\hat{\boldsymbol{e}}_x$ the unit vector in the x-direction; we define $\hat{\boldsymbol{e}}_y$ similarly as the unit vector in the y-direction. Under the assumption that the curvature is a constant value κ, the position vector of such a curve is

$$\boldsymbol{r}(s) = \frac{\sin(\kappa s)}{\kappa}\hat{\boldsymbol{e}}_x + \frac{1-\cos(\kappa s)}{\kappa}\hat{\boldsymbol{e}}_y.$$

As $\kappa \to 0$, this reduces simply to $\boldsymbol{r}(s) = s\hat{\boldsymbol{e}}_x$.
The pitching angle is obtained from the expression

$$\tan\theta_\kappa = \frac{\boldsymbol{r}(1)\cdot\hat{\boldsymbol{e}}_y}{\boldsymbol{r}(1)\cdot\hat{\boldsymbol{e}}_x} = \frac{1-\cos\kappa}{\sin\kappa},$$

which gives

$$\theta_\kappa = \frac{1}{2}\kappa.$$

Further, the length of the chord line (the straight line connecting the leading and trailing edge) is obtained from

$$\sqrt{\boldsymbol{r}(1)\cdot\boldsymbol{r}(1)} = \frac{1}{|\kappa|}\sqrt{2-2\cos(\kappa)} = \frac{\sin(\kappa/2)}{\kappa/2} = \frac{\sin(\theta_\kappa)}{\theta_\kappa}$$

In case of a time-varying κ, the expressions above remain applicable at any instance in time.

References

1. Triantafyllou, G.S., Triantafyllou, M.S., Grosenbaugh, M.A.: Optimal thrust development in oscillating foils with application to fish propulsion. J. Fluids Struct. **7**(2), 205–224 (1993). https://doi.org/10.1006/jfls.1993.1012
2. Smits, A.J.: Undulatory and oscillatory swimming. J. Fluid Mech. **874**, P1 (2019). https://doi.org/10.1017/jfm.2019.284
3. Wu, X., Zhang, X., Tian, X., Li, X., Lu, W.: A review on fluid dynamics of flapping foils. Ocean Eng. **195**, 106712 (2020). https://doi.org/10.1016/j.oceaneng.2019.106712
4. Fish, F.E.: Advantages of aquatic animals as models for bio-inspired drones over present AUV technology. Bioinspir. Biomim. **15**(2), 025001 (2020). https://doi.org/10.1088/1748-3190/ab5a34
5. Nicholson, J.W., Healey, A.J.: The present state of autonomous underwater vehicle (AUV) applications and technologies. Mar. Technol. Soc. J. **42**(1), 44–51 (2008). https://doi.org/10.4031/002533208786861272
6. Bandyopadhyay, P.R.: Swimming and flying in nature-the route toward applications: the freeman scholar lecture. J. Fluids Eng. **131**(3), 031801 (2009). https://doi.org/10.1115/1.3063687
7. Lauder, G.V.: Function of the caudal fin during locomotion in fishes: kinematics, flow visualization and evolutionary patterns. American Zoology **40**(1), 101–122 (2000). https://doi.org/10.1093/icb/40.1.101
8. Fish, F., Lauder, G.V.: Passive and active flow control by swimming fishes and mammals. Annu. Rev. Fluid Mech. **38**(1), 193–224 (2006). https://doi.org/10.1146/annurev.fluid.38.050304.092201
9. Alben, S., Madden, P.G.A., Lauder, G.V.: The mechanics of active fin-shape control in ray-finned fishes. J. R. Soc. Interface **4**(13), 243–256 (2007). https://doi.org/10.1098/rsif.2006.0181
10. Nguyen, K., Yu, N., Bandi, M.M., Venkadesan, M., Mandre, S.: Curvature-induced stiffening of a fish fin. J. R. Soc. Interface **14**(130), 20170247 (2017). https://doi.org/10.1098/rsif.2017.0247
11. Boley, J.W., van Rees, W.M., Lissandrello, C., Horenstein, M.N., Truby, R.L., Kotikian, A., Lewis, J.A., Mahadevan, L.: Shape-shifting structured lattices via multimaterial 4D printing. Proc. Natl. Acad. Sci. **116**(42), 20856–20862 (2019). https://doi.org/10.1073/pnas.1908806116
12. Morales Ferrer, J.M., Sánchez Cruz, R.E., Caplan, S., Van Rees, W.M., Boley, J.W.: Multiscale Heterogeneous Polymer Composites for High Stiffness 4D Printed Electrically Controllable Multifunctional Structures. Adv. Mater. **36**(8), 2307858 (2023). https://doi.org/10.1002/adma.202307858
13. Gazzola, M., van Rees, W.M., Koumoutsakos, P.: C-start: Optimal start of larval fish. J. Fluid Mech. **698**, 5–18 (2012). https://doi.org/10.1017/jfm.2011.558
14. van Rees, W.M., Gazzola, M., Koumoutsakos, P.: Optimal shapes for anguilliform swimmers at intermediate Reynolds numbers. J. Fluid Mech. **722**, 3 (2013). https://doi.org/10.1017/jfm.2013.157
15. van Rees, W.M., Gazzola, M., Koumoutsakos, P.: Optimal morphokinematics for undulatory swimmers at intermediate Reynolds numbers. J. Fluid Mech. **775**, 178–188 (2015). https://doi.org/10.1017/jfm.2015.283

16. Novati, G., Verma, S., Alexeev, D., Rossinelli, D., van Rees, W.M., Koumoutsakos, P.: Synchronisation through learning for two self-propelled swimmers. Bioinspir. Biomim. **12**(3), 036001 (2017). https://doi.org/10.1088/1748-3190/aa6311
17. Mishra, S., van Rees, W.M., Mahadevan, L.: Coordinated crawling via reinforcement learning. J. R. Soc. Interface **17**(169), 20200198 (2020). https://doi.org/10.1098/rsif.2020.0198
18. Katz, J., Weihs, D.: Hydrodynamic propulsion by large amplitude oscillation of an airfoil with chordwise flexibility. J. Fluid Mech. **88**(03), 485 (1978). https://doi.org/10.1017/s0022112078002220
19. Prempraneerach, P., Hover, F.S., Triantafyllou, M.S.: The effect of chordwise flexibility on the thrust and efficiency of a flapping foil. In: 13th international symposium on unmanned untethered submersible technology, vol. 152, pp. 152–170 (2003)
20. Heathcote, S., Gursul, I.: Flexible flapping airfoil propulsion at low reynolds numbers. AIAA J. **45**(5), 1066–1079 (2007). https://doi.org/10.2514/1.25431
21. Dewey, P.A., Boschitsch, B.M., Moored, K.W., Stone, H.A., Smits, A.J.: Scaling laws for the thrust production of flexible pitching panels. J. Fluid Mech. **732**, 29–46 (2013). https://doi.org/10.1017/jfm.2013.384
22. Quinn, D.B., Lauder, G.V., Smits, A.J.: Scaling the propulsive performance of heaving flexible panels. J. Fluid Mech. **738**, 250–267 (2013). https://doi.org/10.1017/jfm.2013.597
23. Quinn, D.B., Lauder, G.V., Smits, A.J.: Maximizing the efficiency of a flexible propulsor using experimental optimization. J. Fluid Mech. **767**, 430–448 (2015). https://doi.org/10.1017/jfm.2015.35
24. Liu, P., Bose, N.: Propulsive performance from oscillating propulsors with spanwise flexibility. Proc. R. Soc. London. Ser. A: Math. Phys. Eng. Sci. **453**(1963), 1763–1770 (1997). https://doi.org/10.1098/rspa.1997.0095
25. Zhu, Q.: Numerical simulation of a flapping foil with chordwise or spanwise flexibility. AIAA J. **45**(10), 2448–2457 (2007). https://doi.org/10.2514/1.28565
26. Zhu, Q., Shoele, K.: Propulsion performance of a skeleton-strengthened fin. J. Exp. Biol. **211**(13), 2087–2100 (2008). https://doi.org/10.1242/jeb.016279
27. Eldredge, J.D., Toomey, J., Medina, A.: On the roles of chord-wise flexibility in a flapping wing with hovering kinematics. J. Fluid Mech. **659**, 94–115 (2010). https://doi.org/10.1017/s0022112010002363
28. Dai, H., Luo, H., De Sousa, P.J.S.A.F., Doyle, J.F.: Thrust performance of a flexible low-aspect-ratio pitching plate. Phys. Fluids **24**(10), 101903 (2012). https://doi.org/10.1063/1.4764047
29. Tian, F.-B., Luo, H., Song, J., Lu, X.-Y.: Force production and asymmetric deformation of a flexible flapping wing in forward flight. J. Fluids Struct. **36**, 149–161 (2013). https://doi.org/10.1016/j.jfluidstructs.2012.07.006
30. Shoele, K., Zhu, Q.: Performance of a wing with nonuniform flexibility in hovering flight. Phys. Fluids **25**(4), 041901 (2013). https://doi.org/10.1063/1.4802193
31. Tytell, E.D., Leftwich, M.C., Hsu, C.-Y., Griffith, B.E., Cohen, A.H., Smits, A.J., Hamlet, C., Fauci, L.J.: Role of body stiffness in undulatory swimming: insights from robotic and computational models. Phys. Rev. Fluids **1**(7), 073202 (2016). https://doi.org/10.1103/physrevfluids.1.073202
32. Wu, T.Y.-T.: Swimming of a waving plate. J. Fluid Mech. **10**(3), 321–344 (1961). https://doi.org/10.1017/s0022112061000949
33. Alben, S.: Optimal flexibility of a flapping appendage in an inviscid fluid. J. Fluid Mech. **614**, 355–380 (2008). https://doi.org/10.1017/S0022112008003297
34. Moore, M.N.J.: Analytical results on the role of flexibility in flapping propulsion. J. Fluid Mech. **757**, 599–612 (2014). https://doi.org/10.1017/jfm.2014.533
35. Floryan, D., Rowley, C.W.: Clarifying the relationship between efficiency and resonance for flexible inertial swimmers. J. Fluid Mech. **853**, 271–300 (2018). https://doi.org/10.1017/jfm.2018.581
36. Moore, M.N.J.: Torsional spring is the optimal flexibility arrangement for thrust production of a flapping wing. Phys. Fluids **27**(9), 091701 (2015). https://doi.org/10.1063/1.4930235
37. Lucas, K.N., Thornycroft, P.J.M., Gemmell, B.J., Colin, S.P., Costello, J.H., Lauder, G.V.: Effects of non-uniform stiffness on the swimming performance of a passively-flexing, fish-like foil model. Bioinspir. Biomim. **10**(5), 056019 (2015). https://doi.org/10.1088/1748-3190/10/5/056019
38. Kancharala, A.K., Philen, M.K.: Optimal chordwise stiffness profiles of self-propelled flapping fins. Bioinspir. Biomim. **11**(5), 056016 (2016). https://doi.org/10.1088/1748-3190/11/5/056016
39. Zhu, Q., Bi, X.: Effects of stiffness distribution and spanwise deformation on the dynamics of a ray-supported caudal fin. Bioinspir. Biomim. **12**(2), 026011 (2017). https://doi.org/10.1088/1748-3190/aa5d3f
40. Wang, W., Huang, H., Lu, X.-Y.: Optimal chordwise stiffness distribution for self-propelled heaving flexible plates. Phys. Fluids **32**(11), 111905 (2020). https://doi.org/10.1063/5.0029806
41. Goza, A., Floryan, D., Rowley, C.: Connections between resonance and nonlinearity in swimming performance of a flexible heaving plate. J. Fluid Mech. **888**, 30 (2020). https://doi.org/10.1017/jfm.2020.60
42. Floryan, D., Rowley, C.W.: Distributed flexibility in inertial swimmers. J. Fluid Mech. **888**, 24 (2020). https://doi.org/10.1017/jfm.2020.49
43. Zheng, C., Ding, J., Dong, B., Lian, G., He, K., Xie, F.: How non-uniform stiffness affects the propulsion performance of a biomimetic robotic fish. Biomimetics **7**(4), 187 (2022). https://doi.org/10.3390/biomimetics7040187
44. Yudin, D., Floryan, D., Van Buren, T.: Propulsive performance of oscillating plates with time-periodic flexibility. J. Fluid Mech. **959**, 31 (2023). https://doi.org/10.1017/jfm.2023.166
45. Neogi, I., Niral Shah, V., Dev Singh, P., Joshi, V.: Propulsion of a combined heaving and trailing-edge morphing foil for bio-inspired applications. Phys. Fluids **35**(4), 043610 (2023). https://doi.org/10.1063/5.0145443
46. Fernández-Gutiérrez, D., van Rees, W.M.: Effect of leading-edge curvature actuation on flapping fin performance. J. Fluid Mech. **921**, A22 (2021). https://doi.org/10.1017/jfm.2021.469
47. Ashraf, M.A., Young, J., Lai, J.C.S.: Oscillation frequency and amplitude effects on plunging airfoil propulsion and flow periodicity. AIAA J. **50**(11), 2308–2324 (2012). https://doi.org/10.2514/1.j051374
48. Martin, N., Gharib, M.: On the role of tip curvature on flapping plates. Bioinspir. Biomim. **13**(2), 026001 (2018). https://doi.org/10.1088/1748-3190/aaa1c0

49. Read, D.A., Hover, F.S., Triantafyllou, M.S.: Forces on oscillating foils for propulsion and maneuvering. J. Fluids Struct. **17**(1), 163–183 (2003). https://doi.org/10.1016/s0889-9746(02)00115-9
50. Angot, P., Bruneau, C.-H., Fabrie, P.: A penalization method to take into account obstacles in incompressible viscous flows. Numer. Math. **81**(4), 497–520 (1999). https://doi.org/10.1007/s002110050401
51. Coquerelle, M., Cottet, G.-H.: A vortex level set method for the two-way coupling of an incompressible fluid with colliding rigid bodies. J. Comput. Phys. **227**(21), 9121–9137 (2008). https://doi.org/10.1016/j.jcp.2008.03.041
52. Gazzola, M., Chatelain, P., van Rees, W.M., Koumoutsakos, P.: Simulations of single and multiple swimmers with non-divergence free deforming geometries. J. Comput. Phys. **230**(19), 7093–7114 (2011). https://doi.org/10.1016/j.jcp.2011.04.025
53. Rossinelli, D., Hejazialhosseini, B., van Rees, W.M., Gazzola, M., Bergdorf, M., Koumoutsakos, P.: MRAG-I2D: multi-resolution adapted grids for remeshed vortex methods on multicore architectures. J. Comput. Phys. **288**, 1–18 (2015). https://doi.org/10.1016/j.jcp.2015.01.035
54. Bernier, C., Gazzola, M., Ronsse, R., Chatelain, P.: Simulations of propelling and energy harvesting articulated bodies via vortex particle-mesh methods. J. Comput. Phys. **392**, 34–55 (2019). https://doi.org/10.1016/j.jcp.2019.04.036
55. van Rees, W.M., Rossinelli, D., Hadjidoukas, P., Koumoutsakos, P.: High performance CPU/GPU multiresolution Poisson solver. In: Bader, M., Bode, A., Bungartz, H.-J., Gerndt, M., Joubert, G.R., Peters, F. (eds.) Parallel Computing: Accelerating Computational Science and Engineering (CSE), pp. 481–490. IOS Press, (2014). https://doi.org/10.3233/978-1-61499-381-0-481
56. van Rees, W.M., Novati, G., Koumoutsakos, P.: Self-propulsion of a counter-rotating cylinder pair in a viscous fluid. Phys. Fluids **27**(6), 063102 (2015). https://doi.org/10.1063/1.4922314
57. Eldredge, J.D., Jones, A.R.: Leading-edge vortices: mechanics and modeling. Annu. Rev. Fluid Mech. **51**(1), 75–104 (2019). https://doi.org/10.1146/annurev-fluid-010518-040334
58. Garrick, I.E.: Propulsion of a flapping and oscillating airfoil. Technical Report 567, National Advisory Committee for Aeronautics, NACA (1936)
59. Taira, K., Colonius, T.: Three-dimensional flows around low-aspect-ratio flat-plate wings at low Reynolds numbers. J. Fluid Mech. **623**, 187–207 (2009). https://doi.org/10.1017/s0022112008005314